Dalton Transactions

ROYAL SOCIETY OF CHEMISTRY

PAPER

View Article Online
View Journal | View Issue

Cite this: *Dalton Trans.*, 2025, **54**, 12516

Charge compensation endows $K_{0.16}Na_{0.05}(NH_4)_{0.71}V_4O_{10-x}\cdot 0.63H_2O$ cathode with tunable lattice strain for efficient Zn^{2+} storage

Xueke Zhu, Dong Fang, * Lang Zhang* and Jianhong Yi

Received 10th June 2025,
Accepted 19th July 2025

DOI: 10.1039/d5dt01363a

rsc.li/dalton

The major challenges in using $NH_4V_4O_{10}$ as a cathode for aqueous zinc-ion batteries (AZIBs) are its unsatisfactory structural stability and carrier migration coefficient due to the accumulated lattice strain during cycling. Herein, we developed a $K_{0.16}Na_{0.05}(NH_4)_{0.71}V_4O_{10-x}\cdot 0.63H_2O$ (NaKNVOH) cathode to achieve a continuous contribution of cathode structure for Zn^{2+} storage at both low and high current density. Both experimental data and DFT calculations confirmed that the charge compensation of Na^+ and K^+ not only reinforced the host structure but also enriched the active sites for Zn^{2+} migration. Especially, the structure-led charge compensation effectively alleviated the lattice strain accumulation during prolonged cycling. The NaKNVOH cathode delivered a specific capacity of 495.4 mAh g^{-1} at 0.5 A g^{-1}, a rate capability of 177.8 mAh g^{-1} at 4 A g^{-1}, and excellent cycle life and capacity retention at current densities of 0.5 A g^{-1} (300 cycles, 94.2%) and 4 A g^{-1} (2000 cycles, 96.57%).

Introduction

Layered $NH_4V_4O_{10}$ (NVO) stands out as a representative vanadium-based cathode for aqueous zinc ion batteries (AZIBs). This can be ascribed to the large ionic radius (143 pm) and small molecular weight (18 g mol^{-1}) of NH_4^+, which contribute to a relatively high capacity (140 mAh g^{-1}).[1–3] The layered structure is stabilized by hydrogen bonds formed between the NH_4^+ pillars and V–O layers, effectively mitigating structural expansion/contraction during the repeated intercalation/extraction process of Zn^{2+}.[3,4] However, the material still suffers from sluggish reaction kinetics, structural distortion and even structural collapse due to the unsatisfactory lattice strain.[5–8] The lattice strain rapidly weakens the interaction between the $[VO_n]$ framework and interlayered "pillars" during the repeated (dis)charging process, especially at low current densities (<1 A g^{-1}).

To address this issue, significant efforts have been made to enhance the electrostatic interaction of the $[VO_n]$ skeleton and limit the invertible extraction of interlayered "pillars" through strategies such as the introduction of guest ions (K^+, Na^+, Ag^+, Cu^{2+}, and Al^{3+}) or molecules (H_2O and C_3N_4), construction of artificial cathode-electrolyte interface layer, and optimization of electrolytes.[3,9–14] Among these, pre-intercalating heterocations have been shown to enhance the stability of the lattice structure and reduce the energy barrier in layered cathodes during electrochemical reactions.[12,15] The regulation of the covalent degree's effect on the mean charge of lattice oxygen by pre-intercalated metal-ions, resulting in an improved Zn^{2+} diffusion kinetics. Particularly, alkali metal cations (M^+, M = Li, Na, and K) endow NVO with tunable structural integrity and satisfactory electrochemical kinetics derived from their different ionic radii and masses.[16,17] A previous work has demonstrated that the sole incorporation of K^+ results in low electronic conductivity, leading to significantly inadequate rate capability. Concurrently, the relatively weak structural stability causes noticeable capacity fading during long-term cycling.[16] Under this background, the charge compensation effect between dual cations (such as Na^+ and K^+) may effectively alleviate lattice strain accumulation during prolonged cycling, thereby significantly reducing the diffusion energy barrier of Zn^{2+} and promoting cycle stability at both high and low current densities.[16–19]

Herein, we developed a medium-entropy $K_{0.16}Na_{0.05}(NH_4)_{0.71}V_4O_{10-x}\cdot 0.63H_2O$ (NaKNVOH) nanowire by utilizing the regulatory effect of "Na^+–K^+-in-subsequence" for efficient Zn^{2+} storage. Unlike single Na^+ ion intercalation, Na^+–K^+-in-subsequence expands the interlayer spacing and reduces the migration energy barrier, facilitating efficient Zn^{2+} transport. In addition, the charge compensation effect between Na^+ and K^+ effectively alleviates lattice strain. The NaKNVOH cathode delivers a high specific capacity of 336.0 mAh g^{-1} at 0.5 A g^{-1} with outstanding rate capability (177.8 mAh g^{-1} at 4 A g^{-1}) and excellent cycling stability at current densities of 0.5 and 4 A g^{-1}. Furthermore, the positive Zn^{2+}/H^+ migration mechanism in NaKNVOH has been confirmed

Faculty of Materials Science and Engineering, Kunming University of Science and Technology, Kunming, 650093, P. R. China. E-mail: fangdong@kmust.edu.cn, 3086818048@qq.com

by *in situ* XRD analysis and DFT calculation, which is of great significance for the construction of high-performance layered cathode for AZIBs.

Experimental sections

Synthesis of NaKNVOH and NaNVOH nanowires

All chemicals were of analytical grade and used without further purification. All samples were prepared *via* a simple hydrothermal method. In detail, 6 g $H_2C_2O_4$, 0.63 g $C_6H_{12}N_4$, 4.64 g NH_4VO_3, 0.29 g NaCl (0.005 M) and 0.37 g KCl (0.005 M) were added into a mixed solution consisting of 145 mL deionized water and 30 mL ethanol and heated in a 50 °C water bath with stirring for 4 h. Several pieces of titanium foil and 90 mL of the supernatant liquid were dipped directly in a 100 mL Teflon-lined stainless-steel autoclave heated at 120 °C for 1 h to obtain NaKNVOH. The NaNVOH are synthesized by only 0.59 g NaCl (0.01 M) compared with NaKNVOH. The titanium foil loaded with the active material was washed with deionized water and dried at 80 °C for 6 h, and the mass loading was ~1.3 mg.

Material characterizations

X-ray diffraction (XRD) data were collected using a Rigaku Miniflex 600 X-ray diffractometer equipped with Cu Kα radiation (λ = 1.5418 Å). The morphology and structure were recorded using field emission scanning electron microscopy (ZEISS, Gemini SEM 300) and transmission electron microscopy (TEM, FEI Talos F200X) with an EDS (FEI Super-X EDS Detector). Fourier transform infrared spectroscopy (FTIR) patterns were collected on DTGs KBr with scanning from 4000 to 400 cm^{-1}. Raman spectra were conducted on Renishaw inVia at room temperature. Thermogravimetric (TG-DSC) analysis was performed on a HITACHI STA200 thermal analyzer with a heating rate of 10 °C min^{-1} under an air atmosphere from 30 to 500 °C. Inductively coupled plasma mass spectrometry (ICP-OES, Agilent) and oxygen/nitrogen/hydrogen analyzer (ONH836) were performed to determine the chemical composition. The electron paramagnetic resonance (EPR German Bruker EMXplus-6/1) was used to study the oxygen vacancies. X-ray photoelectron spectroscopy (XPS) was performed on an X-ray photoelectron spectrometer (Thermo ESCALAB 250Xi) with Al Kα ($h\nu$ = 1486.6 eV). Besides, the test parameters of the *in situ* XRD patterns were 2° min^{-1} (scan rate) and 0.02° (step size).

Electrochemical characterization

To test the electrochemical performance, coin cells were assembled. The working cathodes comprise titanium circle sheets (d = 14 mm) loaded with active species (NaNVOH and NaKNVOH) to fabricate CR2025 coin-type cells in an ambient atmosphere, in which glass fiber served as the separator, zinc foil acted as the anode, and 3 M $Zn(CF_3SO_3)_2$ as the electrolyte. Cyclic voltammetry (CV) curves in a voltage window of 0.2–1.6 V and electrochemical impedance spectra (EIS) in the frequency range of 0.01–100 000 Hz were recorded using an electrochemical workstation (CHI 760E, Shanghai Chenhua Company, PR China). The galvanostatic discharge charge (GDC) and the galvanostatic intermittent titration technique (GITT) were performed utilizing a battery test system (NEWARE, PR China). The capacity fluctuations during cycling arise from variations in the ambient temperature.[20] The Zn-ion diffusion coefficient can be calculated using the following equation:

$$D = \frac{4L^2}{\pi\tau}\left(\frac{\Delta E_s}{\Delta E_\tau}\right)^2$$

L is the diffusion depth of Zn^{2+}, τ is the constant current pulse time, and ΔE_s and ΔE_τ are the voltage changes during intermittent charging and discharging.[20]

Computational methods

Theoretical calculations were based on density functional theory (DFT) and implemented using the Vienna *ab initio* simulation package (VASP).[21] The exchange–correlation interaction was described by the Perdew–Burke–Ernzerhof (PBE) functional.[22] The 1 × 2 × 1 supercell was constructed using a layered model of $NH_4V_4O_{10}$ (a × b × c, 11.807 × 3.675 × 10.305 $Å^3$) to investigate the Zn^{2+}/H^+ storage ability and structural stability. In this calculation, oxygen vacancies, doping Na^+, and crystal water were considered. Specifically, the content of Na^+ in the three models was constant, while the contents of H_2O, NH_4^+ and oxygen vacancy were varied. The plane-wave basis was set with an energy cutoff of 450 eV and the projector-augmented plane-wave (PAW) method was used. The convergence criteria for electronic relaxation and ion relaxation were 1.0×10^{-5} eV and −0.05 eV $Å^{-1}$, respectively. The DFT+U was applied, and the value of U was set as 3.25 eV to correct the strong interactions of V 3d electrons.[23] Meanwhile, DFT-D3 correction was used to describe van der Waals interactions. Figure illustrations were done with the help of VESTA software.

Results and discussion

Structural features

X-ray diffraction (XRD) patterns of NaNVOH and NaKNVOH are compared in Fig. 1a. All diffraction peaks can be indexed to the monoclinic $NH_4V_4O_{10}$ (JCPDS no. 31-0075), which belongs to the $C2/m$ space group and lattice parameters a = 11.71 Å, b = 3.66 Å, c = 9.72 Å, β = 101.0°. This indicates that the insertion of impurities has not altered the layered structure.[24] According to the Bragg equation, the (001) diffraction peak of NaKNVOH (8.0°) shifts to a lower degree compared to NaNVOH (8.5°), suggesting an expansion of interplanar spacing. The FTIR spectra of NaNVOH and NaKNVOH in Fig. 1b are similar to that of $NH_4V_4O_{10}$, further illustrating the similar layered [VO_n] framework. The peak at 555 cm^{-1} corresponds to the V–O bending mode,[25] while the peak at 753 cm^{-1} is assigned to the asymmetric V–O–V stretching mode.[26] The

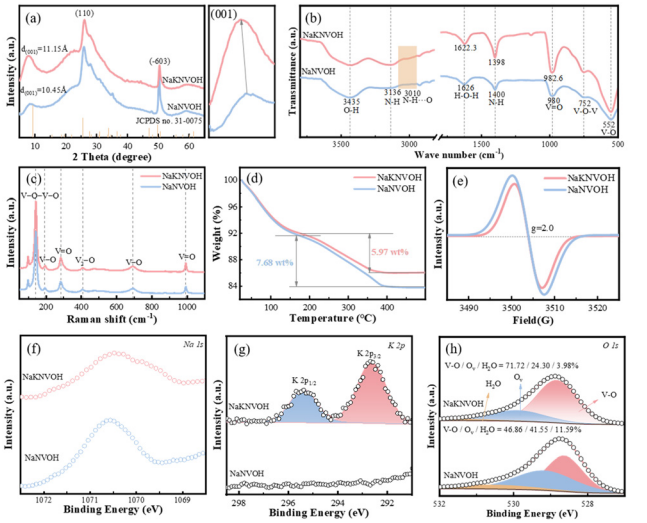

Fig. 1 Phase and structural characterizations of NaNVOH and NaKNVOH. (a) XRD patterns and the enlarged patterns of the (001) plane. (b) FTIR spectra. (c) Raman spectra. (d) TG curves. (e) EPR patterns. (f) Na 1s, (g) K 2p, and (h) O 1s high-resolution XPS spectra.

characteristic peak at 983 cm^{-1} represents the tensile vibration of V=O.[25] The peaks observed at 1403 cm^{-1} and 3136 cm^{-1} are attributed to the bending and stretching vibrations of the N–H bonds.[27] The peaks at 1625 cm^{-1} and 3435 cm^{-1} indicate the stretching modes of crystal water present in NaNVOH and NaKNVOH. Additionally, a peak at 3010 cm^{-1} in NaKNVOH suggests the formation of hydrogen bonds (N–H···O) with some covalent character between the [VO_n] and NH_4^+ layers, which contributes to the stability of the layered structure.[28] Upon careful inspection, NaKNVOH exhibits a redshift of 3.7 cm^{-1} for the H–O–H bending mode and 2 cm^{-1} for the N–H stretching mode, which is related to the modified interaction between H_2O and NH_4^+.[29] In the Raman spectra (Fig. 1c), the peaks at 285 and 994 cm^{-1} are attributed to the bending and stretching vibration modes of the V=O double bond.[30] The peaks at 193 and 694 cm^{-1} represent the stretching vibration of V–O bonds. The peak at 408 cm^{-1} corresponds to the stretching vibration of the V_2–O bonds.[31] The peak at 140 cm^{-1} is associated with the bending vibration of the –V–O–V–O– chains, indicating a long-range ordered structure related to the layered configuration.[32] To verify the effects of single Na^+ intercalation or co-insertion of K^+ and Na^+, thermogravimetric (TG) and electron paramagnetic resonance (EPR) analyses were performed. The TG curves for NaNVOH and NaKNVOH are presented in Fig. 1d. The initial weight loss corresponds to the desorption of physically adsorbed water. The subsequent weight loss represents the release of crystal water and ammonium ions. The final stage involves the complete removal of ammonium ions accompanied by a crystallization process. Notably, the total mass losses corresponding to NH_4^+ and crystalline water were measured as 7.68% and 5.97% for NaNVOH and NaKNVOH, respectively. Both samples exhibit an EPR signal with a g value of 2.0, indicating the presence of V^{4+} ions (Fig. 1e).[33,34] The vibration in intensity is due to the different proportion of V^{4+} and oxygen vacancies. The higher signal intensity observed in NaNVOH suggests a higher ratio of V^{4+} ions and oxygen vacancies. This phenomenon arises because the sole incorporation of Na^+ into the [VO_n] layers induces localized charge imbalance. To maintain electro neutrality, the system compensates for the positive charge deficiency through oxygen vacancy formation (*via* O^{2-} elimination). The synergistic incorporation of K^+ and Na^+ achieves balanced charge compensation across distinct lattice sites, significantly reducing the reliance on oxygen vacancy generation.[35] The contents of K, Na, V, and N in both samples were quantified by inductively coupled plasma optical emission spectrometry (ICP-OES) analysis and an oxygen/nitrogen/hydrogen analyzer (ONH), as depicted in Table S1. The chemical formulas of NaNVOH and NaKNVOH were determined to be $Na_{0.10}(NH_4)_{1.04}V_4O_{10-y}\cdot 0.52H_2O$ and $K_{0.16}Na_{0.05}(NH_4)_{0.71}V_4O_{10-x}\cdot 0.63H_2O$, respectively.

The chemical states of NaNVOH and NaKNVOH were further investigated by X-ray photoelectron spectroscopy (XPS) (comprehensive XPS spectra in Fig. S1). In the V 2p spectrum (Fig. 1f), the co-doping of K^+ and Na^+ increases the proportion of V^{4+} from 11.30% to 30.15%. It demonstrates that the charge compensation mechanism for K^+ and Na^+ involves the reduction of some vanadium ions (V^{5+}) to the lower valence state (V^{4+}) for maintaining charge neutrality.[36] In the O 1s spectra (Fig. 1g), the binding energies of 531.55 eV, 529.90 eV, and 528.84 eV are attributed to absorbed H_2O, oxygen vacancies (O_v), and lattice oxygen, respectively. High-resolution K 2p (Fig. 1h) and Na 1s (Fig. S2a) spectra confirm the co-intercalation of K^+ and Na^+ in NaKNVOH, while only Na^+ is inserted in NaNVOH. Additionally, the broadening of the Na 1s peak in NaKNVOH is attributed to the different sodium environment.[37] In the N 1s spectra (Fig. S2b), the signal corresponds to –NH– (398.26 eV) and $-N^+H-$ (400.14 eV). Furthermore, the shift of the V 2p peak towards lower binding energy and the shifting of the O 1s and N 1s peaks to higher binding energies after dual-ion doping further demonstrate that it induces a secondary electronic rearrangement in the local chemical environment.

Scanning electron microscopy (SEM) and transmission electron microscopy (TEM) images of NaKNVOH (Fig. S2a and b) show that it grows uniformly on titanium foil, forming nanowire arrays. In addition, the morphology of NaKNVOH is similar to that of NaNVOH (Fig. S3a and b), indicating that the incorporation of K^+ does not change the morphology. EDS mapping in Fig. 2c demonstrates that the K, Na, N, V, and O elements are uniformly distributed throughout the entire nanobelt, while NaNVOH only shows Na, N, V, and O elements (Fig. S3c), further confirming the controllable introduction of alkali metal ions. The high-resolution TEM (HRTEM) images of NaNVOH (Fig. 2d) exhibit lattice spacings of 2.97 Å and 1.77 Å corresponding to the (112) and (−603) planes in the [1–52] zone axis, as confirmed by fast Fourier transform (FFT) and inverse fast Fourier transform (IFFT) analyses (Fig. 2f). The HRTEM images of NaKNVOH (Fig. 2e) show lattice spacings of 3.23 Å and 1.82 Å along the [−101] zone axis for the (111) and (020)

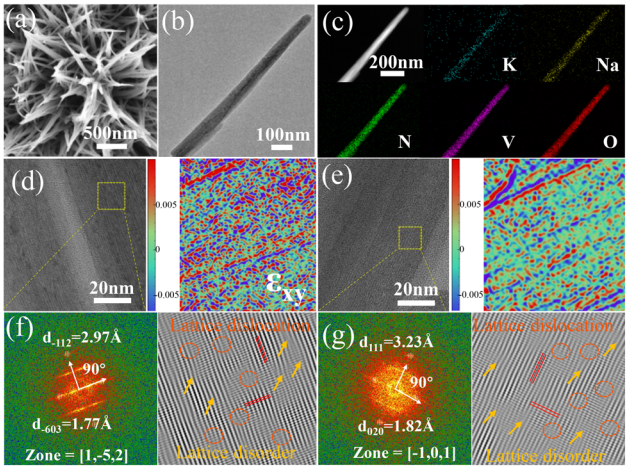

Fig. 2 (a) SEM, (b) TEM, and (c) HAADF and EDS-mapping images of NaKNVOH. HRTEM and the corresponding GPA images of strain along the xy direction of (d) NaNVOH and (e) NaKNVOH. FFT and IFFT images of (f) NaNVOH and (g) NaKNVOH.

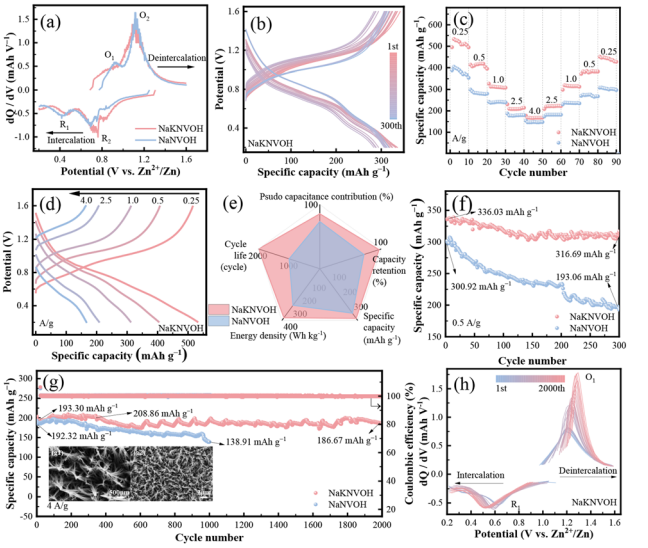

Fig. 3 Electrochemical performance of AZIBs based on NaNVOH and NaKNVOH. (a) dQ/dV plots. (b) GCD curves at 0.5 A g^{-1}. (c) Rate performance. (d) GCD curves of NaKNVOH at various current densities. (e) Radar plots. (f) Cycling performance at a current density of 0.5 A g^{-1}. (g) Cycling performance at a current density of 4.0 A g^{-1}; inset: (g1, g2) SEM images of NaKNVOH. (h) dQ/dV plots of NaKNVOH at a current density of 4.0 A g^{-1}.

planes (Fig. 2g). Additionally, geometric phase analysis (GPA) was used to assess the strain distributions.[38] Compared with NaNVOH (Fig. 2e), the strain distribution of NaKNVOH (Fig. 2f) along the *xy* axis is more homogeneous with the intercalation of Na^+–K^+-in-subsequenced, which can mitigate structural collapse caused by localized lattice distortions.[39]

Electrochemical performance

Fig. S4a and b depict the initial three cyclic voltammetry (CV) cycles of NaNVOH and NaKNVOH at a scan rate of 0.2 mV s^{-1}. The overlap of the CV curves during the second and third cycles indicates the establishment of a reversible redox reaction after the initial activation cycle. A comparison of CV curves for NaNVOH//Zn and NaKNVOH//Zn at the same scan rate is shown in Fig. S4c. NaKNVOH//Zn exhibits a higher response current at the V^{5+}/V^{4+} redox peaks and a larger CV area, suggesting that Zn^{2+} ions are more easily intercalated between the layers, thereby providing a greater specific capacity compared to NaNVOH//Zn. When subjected to a current density of 0.5 A g^{-1}, both cathodes exhibit two distinct peaks in the dQ/dV plots (Fig. 3a), which are consistent with their CV results.[40] The galvanostatic charge–discharge (GCD) profiles of NaNVOH and NaKNVOH at 0.5 A g^{-1} are presented in Fig. 3b and further analyzed in conjunction with the dQ/dV plots.[31] In the first step (marked by R_2), the reduction of V^{5+} to V^{4+} in NaKNVOH delivers a capacity of 130 mAh g^{-1}, which is higher than that of NaNVOH (110 mAh g^{-1}). This enhancement is attributed to the complete reduction of V^{5+} and improved diffusion kinetics in NaKNVOH. In the second step (labeled R_1), the V^{4+} derived from the first step in NaKNVOH, along with intrinsic V^{4+} ions, is reduced to V^{3+}, yielding a capacity of 250 mAh g^{-1} (compared to 230 mAh g^{-1} for NaNVOH). This indicates that the activated V^{4+}/V^{3+} redox reaction in NaKNVOH during Zn^{2+} (de)intercalation contributes to the increased capacity.[41]

The advantages of the "Na^+–K^+-in-subsequence" strategy in the material are clarified through a comparative assessment of the rate performance and cycling stability of NaNVOH//Zn and NaKNVOH//Zn batteries. The NaKNVOH cathodes exhibit specific capacities (Fig. 3c) of 495.4, 414.2, 327.1, 230.6, and 177.8 mAh g^{-1} at current densities of 0.25, 0.5, 1.0, 2.5, and 4.0 A g^{-1}, as determined from GCD profiles depicted in Fig. 3d. When the current densities are reverted to 2.5, 1.0, 0.5, and 0.25 A g^{-1}, the discharge capacities recover to 208.4, 298.4, 372.6, and 451.3 mAh g^{-1}. NaKNVOH//Zn demonstrates a superior rate capability with higher specific capacities compared to NaNVOH//Zn (Fig. 3c and S4) at equivalent current densities. After returning to the initial current density, the capacity retention rate of NaKNVOH is 91%, while that of NaNVOH is only 79%, highlighting the robust tolerance of NaKNVOH to rapid Zn^{2+} (de)intercalation. Fig. 3f shows the cycling performance of the two cells at a low current density of 0.5 A g^{-1}. The initial specific capacity of the NaKNVOH cathode is 336.03 mAh g^{-1}, and after 300 cycles, it retains a specific capacity of 316.69 mAh g^{-1}, corresponding to a capacity retention rate of 94.2%. This is significantly higher than the capacity retention rate of the NaNVOH//Zn battery, which is 64% with an initial specific capacity of 300.92 mAh g^{-1}. The GCD curves of NaKNVOH are shown in Fig. S5a, with a gradient from pink to blue visually demonstrating this stability compared to NaNVOH (Fig. S5b). The long-term cycling performance of the two electrodes was further tested at a high current density of 4.0 A g^{-1}. As shown in Fig. 3g, the NaKNVOH cathode exhibits an initial discharge capacity of 193.30 mAh g^{-1}, which gradually increases to 208.86 mAh g^{-1}

after 230 cycles. This increase can be attributed to infiltration and electrochemical activation processes,[42,43] a phenomenon also observed in previous studies on layered vanadate and manganite.[44,45] Subsequently, the capacity stabilizes at 186.67 mAh g^{-1} after 2000 cycles, yielding a high capacity retention rate of 96.57% with a coulombic efficiency (CE) close to 100%. However, the fluctuations during cycling are due to changes in ambient temperature.[20] SEM images of the NaKNVOH cathode in its initial state and after 2000 cycles (Fig. 3g1 and g2) confirm that the nanowire morphology remains well-preserved. Additionally, the XRD pattern of NaKNVOH after 2000 cycles (Fig. S6) shows almost no byproducts. In contrast, NaNVOH electrode exhibits rapid capacity decay after initial fluctuations, starting from 192.32 mAh g^{-1}, with only 72.23% capacity retention after 1000 cycles. Fig. S8 and Fig. 3h present the dQ/dV analysis of NaNVOH and NaKNVOH cathodes after 2000 cycles at 4 A g^{-1}. At high current densities, both cathodes exhibit two distinct peaks: an oxidation peak (O_1) at ~1.3 V (V^{5+}) and a reduction peak (R_1) at ~0.6 V (V^{3+}). As the number of cycles increases, O_1 shifts to a higher voltage and R_1 shifts to a lower voltage due to polarization. The intensity of O_1 gradually increases, with NaKNVOH showing a higher dQ/dV peak than NaNVOH. This suggests that the gradual activation of NaKNVOH results in more active sites, enhancing the reaction rate. The observed fluctuating capacity can be attributed to variations in the diffusion-controlled contribution, which are influenced by changes in interlayer spacing and environmental temperature, ultimately leading to capacity fluctuations.[45] In addition, to further present the superiority of NaKNVOH//Zn battery, their performances were compared with those of the previously reported ammonium vanadate (Fig. 3e), including $(NH_4)_2V_{10}O_{25}{\cdot}8H_2O$ and NVO. NaNVOH cathode possesses better comprehensive performance.[46,47]

The charge storage mechanisms of NaKNVOH//Zn and NaNVOH//Zn batteries are investigated through comprehensive electrochemical kinetic analysis. As illustrated in Fig. 4a, the cyclic voltammetry (CV) scanning rate is increased from 0.2 mV s^{-1} to 1.0 mV s^{-1}. The observed slight peak shift is attributed to polarization effects during Zn^{2+} (de)intercalation processes. Furthermore, the well-shaped V^{4+}/V^{3+}peak (pointed out by the black arrow) of NaKNVOH also verifies that the Na^+–K^+-in-subsequence effectively facilitates the multivalent redox transitions of $V^{5+}/V^{4+}/V^{3+}$, thereby reducing the potential gap between oxidation and reduction and improving the reversible transformation of the [VO_n] layer.[48–50] The relationship between the peak current (i) and scan rate (v) is described by the power-law equation:[51,52]

$$i = av^b \quad (1)$$

The constants a and b represent the empirical parameters; the value of b is defined by the slopes of log(i) *vs.* log(v), as shown in the following equation:

$$\log(i) = b \cdot \log(v) + \log(a) \quad (2)$$

In general, the value of b ranges from 0.5 to 1. A b-value of 0.5 suggests that the electrochemical behavior is solely governed by diffusion control, whereas a b-value of 1 indicates that the capacitive behavior is dominant. The b-value fitting curves for NaNVOH and NaKNVOH electrodes are presented in Fig. 4b. The b-values for the first and second peaks of NaKNVOH are 0.75 and 1.00, while both peaks of NaNVOH exhibit a b-value of 0.83. These results indicate that the charge storage mechanism of the cathode materials is primarily based on the combined action of pseudocapacitance and diffusion behavior. To further investigate the ratio in the total capacity, the pseudo-capacitive contribution ratio can be calculated by the formula:

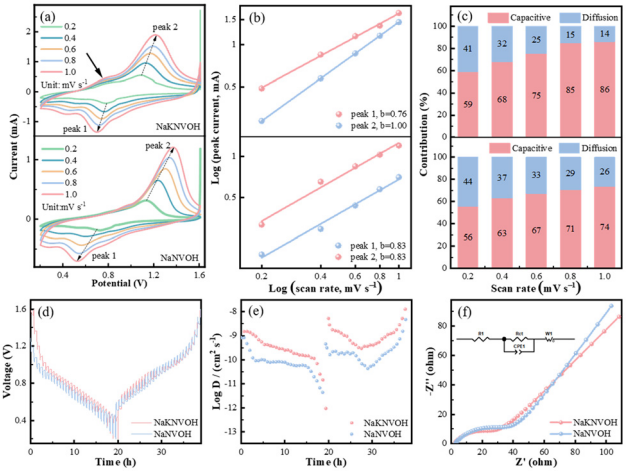

Fig. 4 Electrochemical kinetic mechanism of NaNVOH and NaKNVOH cathodes. (a) CV curves at different scan rates. (b) Relationship between peak currents and scan rates. (c) Pseudocapacitive contribution at various scan rates. (d) GITT curves and (e) calculated diffusion coefficients of Zn^{2+}. (f) EIS spectra with fitted equivalent circuit diagrams.

$$i = k_1v + k_2v^{\frac{1}{2}} \quad (3)$$

where k_1v represents the capacitance effect and $k_2v^{\frac{1}{2}}$ corresponds to diffusion-controlled behavior. Fig. 4c displays the capacitance contribution within the scan rate range of 0.2 to 1.0 mV s^{-1}. As the scan rate increases, the percentage of capacitance contribution for NaKNVOH (increases from 59% to 86%) is higher than that for NaNVOH (increases from 56% to 74%).

The diffusion kinetics of Zn^{2+} in the lattice of NaNVOH and NaKNVOH during cycling is further studied *via* GITT measurements (Fig. 4d and e). The diffusion coefficient values of NaKNVOH ($10^{-7.9}$–$10^{-10.8}$) are higher than those of NaNVOH ($10^{-8.3}$–$10^{-11.4}$) during the entire discharging/charging process. It is worth noting that the sharp decline in the diffusion coefficient of NaKNVOH at the final point of discharge may be attributed to minor interfacial side reactions. In addition, as depicted in Fig. 4f, the diameter of the semicircle in the high-frequency region of the electrochemical impedance spectroscopy (EIS) plot is indicative of the charge transfer resistance (R_{ct}). According to the fitting results of the equivalent circuit model, the R_{ct} value for NaKNVOH electrode is deter-

mined to be 28.16 Ω, which is smaller than that of NaNVOH cathode, which has an R_{ct} of 37.1 Ω.

Charge transfer mechanism

The phase structure of NaKNVOH during the first two discharge–charge cycles is investigated by *in situ* XRD tests, as shown in Fig. S9 and Fig. 5a. The diffraction peak observed at 22° corresponds to the characteristic peak of the carbon paper collector. No obvious new peaks emerge during the two (dis) charging processes, revealing that NaKNVOH has a single-phase structure during cycling. The diffraction signals of the (001), (−402), (004), and (−315) planes shift during the discharge–charge cycles. Specifically, with the increase of discharge depth, the peaks shift towards a lower angle and revert to a higher angle after charging; this shrinkage and enlargement of the interlayer demonstrate the reversible insertion/extraction. The increasing interplanar spacing during the discharging process is due to the co-intercalation of H_2O and Zn^{2+}, which serves to mitigate the effective charge interactions between Zn^{2+} and defect-free V–O.[53,54] In contrast, the slight shift of the (001) plane and substantial shift of the (−312) and (−315) planes indicate that the lattice strain along the *c*-axis is improved during the repeated (dis)charging process; the schematic diagram of the three planes is shown in Fig. 5b.

The evolution of morphology and chemical states of the NaKNVOH cathode in different (dis)charging states is investigated *via* SEM-EDS mapping and XPS analysis. As shown in Fig. S10–S12, NaNVOH electrode exhibits partial fracture of its 3D architecture upon discharging, followed by structural collapse upon recharging to 1.6 V, whereas NaKNVOH maintains an intact 3D nanowire network throughout the entire discharge/charge process. As illustrated in Fig. 5c, the initial NaKNVOH cathode exhibits distinct Zn signals. Upon full discharge to 0.2 V, a significant enhancement in the Zn 2p peak intensity is observed, confirming more Zn^{2+} intercalation. When charged to 1.6 V, the Zn 2p peak intensity diminished, indicating the extraction of Zn^{2+} from the host structure. The V 2p spectra (Fig. 5d) reveal a decrease in the V^{5+} peak intensity, accompanied by the emergence of a V^{3+} peak upon discharge to 0.2 V, demonstrating a two-step reduction reaction from V^{5+} to V^{3+}. Subsequent charging to 1.6 V restores the V^{5+} peak intensity while eliminating the V^{3+} signal, achieving near-identical spectral features to those of the pristine state. For the O 1s spectra (Fig. 5e), the intensity of the oxygen vacancy (O_v) peak decreases upon discharge to 0.2 V, concurrent with an increase in the H_2O-related peak intensity. Moreover, the N 1s, K 2p, and Na 1s spectra (Fig. S13) verify that NH_4^+, K^+, and Na^+ exist stably during cycling. The reversible shift of the Na 1s peak to a lower binding energy during discharge and its recovery upon charging originates from the dynamic charge redistribution within the cathode framework. It suggests that the insertion/extraction of Zn^{2+} in NaKNVOH is reversible.

Density functional theory (DFT) calculations were conducted to clarify the impacts of K–Na dual ion and reveal the diffusion pathway and diffusion energy barriers of Zn^{2+} in NaNVOH and NaKNVOH. The geometrically optimized crystal structure is shown in Fig. 6a. The enlarged *c*-value of 10.64 Å compared to NaNVOH (10.51 Å) indicates that K^+ intercalation weakens the compressive stress. The total density of states (DOS) (Fig. 6b) indicates that NaKNVOH displays a new electronic state and a lower conduction energy, suggesting optimized carrier migration efficiency, thus contributing to high capacity. Charge density difference analysis of NaNVOH and NaKNVOH (Fig. 6c) was performed to investigate the modulation of the electron structure. The negative charge distri-

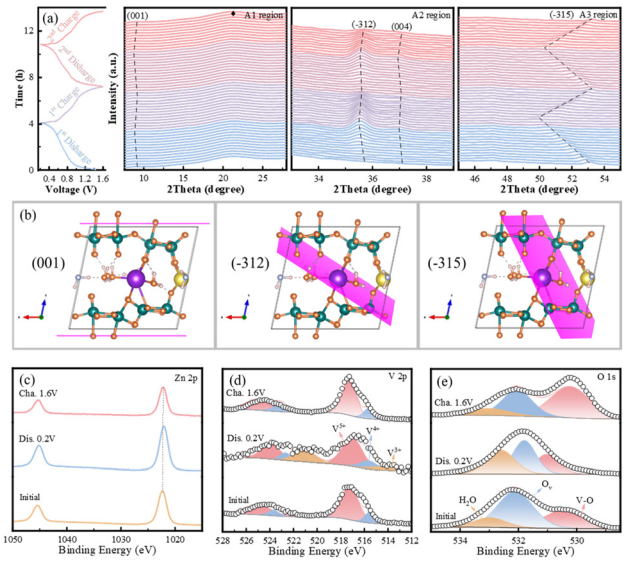

Fig. 5 (a) GCD profiles of the first two cycles of NaKNVOH cathode and the corresponding *in situ* XRD patterns. (b) Schematic of (001), (−312), and (−315) planes for NaKNVOH. *Ex situ* high-resolution XPS spectra of (c) Zn 2p, (d) V 2p, and (e) O 1s.

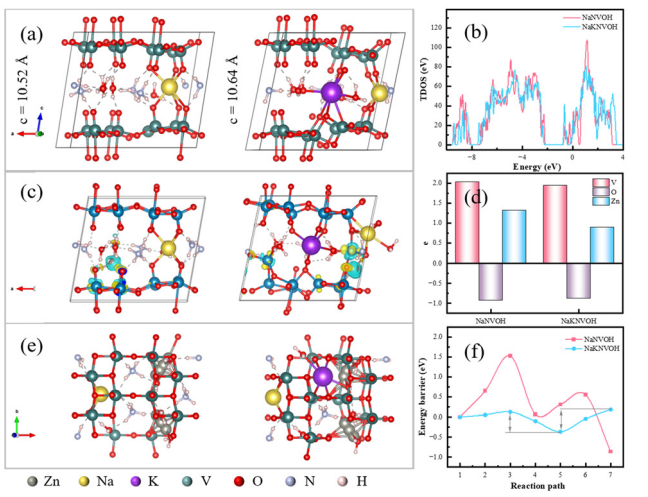

Fig. 6 DFT calculation results of NaNVOH and NaKNVOH. (a) The crystal structures viewed along the b-axis and (b) corresponding TDOS spectra (the Fermi level is set at zero). (c) Charge density difference analysis and (d) average Bader charge of V, O, and Zn. (e) Possible Zn^{2+} diffusion pathways and (f) calculated diffusion barriers.

bution shifts toward the V atoms due to structural regulation, resulting in weaker electrostatic interactions between zinc ions and [VO_n] layers during the zinc ion intercalation, thereby facilitating the diffusion kinetics. The top view of possible migration pathways for Zn^{2+} in NaNVOH and NaKNVOH is shown in Fig. 6e, where Zn^{2+} mainly diffuses along the *b*-axis as reported in similar studies.[55] The energy barrier along the Zn^{2+} migration pathway for KNVO is approximately 0.55 eV in Fig. 6f, which is lower than that of NVO (~2.39 eV), suggesting that Na^+–K^+-in-sequence optimizes the pathway and promotes faster Zn^{2+} migration.[24]

Conclusions

In summary, we obtained a high-performance $K_{0.16}Na_{0.05}(NH_4)_{0.71}V_4O_{10-x}{\cdot}0.63H_2O$ nanowire cathode for AZIBs, synthesized by the "Na^+–K^+-in-subsequence" strategy. Na^+ and K^+ enlarge the interlayer spacing, reduce the migration energy barrier for Zn^{2+} ions, and the charge compensation effect between Na^+ and K^+ effectively alleviates lattice strain accumulation during prolonged cycling. Notably, the intercalation of extra H_2O to form a water shielding layer results in fewer Zn^{2+} remaining on the crystal planes along the *c*-axis, ensuring efficient Zn^{2+} transport. As a result, the NaKNVOH cathode delivers a high specific capacity of 336.03 mAh g^{-1} at 0.5 A g^{-1} with outstanding rate capability (177.77 mAh g^{-1} at 4 A g^{-1}), and excellent cycling stability and capacity retention at a current density of 0.5 A g^{-1} (300 cycles, 94.2%) and 4 A g^{-1} (2000 cycles, 96.57%). This work is of great significance for the reconstruction of high-performance layered cathodes for AZIBs.

Author contributions

Xueke Zhu: writing – original draft, review and editing, software, methodology, investigation. Dong Fang: writing – review and editing, project administration, resources, conceptualization. Lang Zhang: writing – review and editing, supervision, project administration, conceptualization. Jianhong Yi: writing – review and editing, project administration, conceptualization.

Conflicts of interest

There are no conflicts to declare.

Data availability

The data supporting this article have been included as part of the SI.

Supplementary information (Fig. S1–S13) is available. See DOI: https://doi.org/10.1039/d5dt01363a.

Acknowledgements

This work was supported by the fund of the Major Special Projects in Yunnan Province (No. 202302AG050007, 202302AH360001) and Yunnan Provincial Key Laboratory of Metallurgy Science and Technology Program (TPIL-20040602060).

References

1 T. He, Y. Ye, H. Li, S. Weng and B. Wang, *Mater. Today*, 2021, **43**, 53–61.
2 H. Xiao, R. Li, L. Zhu, X. Chen, L. Xie, Q. Han, X. Qiu, L. Yi and X. Cao, *J. Energy Storage*, 2024, **89**, 111640.
3 B. Tang, J. Zhou, G. Fang, F. Liu, C. Zhu, C. Wang, A. Pan and S. Liang, *J. Mater. Chem. A*, 2019, **7**, 940–945.
4 M. Huang, Y. Mai, L. Zhao, X. Liang, Z. Fang and X. Jie, *ChemElectroChem*, 2020, **7**, 4218–4223.
5 Y. Zeng, X. F. Lu, S. L. Zhang, D. Luan, S. Li and X. W. Lou, *Angew. Chem., Int. Ed.*, 2021, **60**, 22189–22194.
6 L. Cheng, Y. Huang, S. Yin, M. Chen, Y. Liu, Y. Zhang, F. Seidi, Z. Lin and H. Xiao, *Carbohydr. Polym.*, 2023, **316**, 121075.
7 F. Ye, Q. Liu, H. Dong, K. Guan, Z. Chen, N. Ju and L. Hu, *Angew. Chem., Int. Ed.*, 2022, **61**, e202214244.
8 W. Shi, W. S. V. Lee and J. Xue, *ChemSusChem*, 2021, **14**, 1634–1658.
9 T. Qiu, T. Wang, W. Tang, Y. Li, Y. Li, X. Lang, Q. Jiang and H. Tan, *Angew. Chem., Int. Ed.*, 2023, **62**, e202312020.
10 Z. Su, R. H. Wang, J. H. Huang, R. Sun, Z. Qin, Y. F. Zhang and H. Fan, *Rare Met.*, 2022, **41**, 2844–2852.
11 M. Li, Y. Zhang, J. Hu, X. Wang, J. Zhu, C. Niu, C. Han and L. Mai, *Nano Energy*, 2022, **100**, 107539.
12 H. Jiang, Y. Zhang, L. Xu, Z. Gao, J. Zheng, Q. Wang, C. Meng and J. Wang, *Mater. Today Energy*, 2021, **382**, 122844.
13 D. He, Y. Peng, Y. Ding, X. Xu and L. Hu, *J. Power Sources*, 2021, **484**, 229284.
14 Q. Wang, J. Wu, M. Wang, H. Yu, X. Qiu and W. Chen, *Adv. Sci.*, 2024, **11**, 2307872.
15 T. Boya, F. Guozhao, Z. Jiang, W. Liangbing, L. Yongpeng, W. Chao, L. Tianquan, T. Yan and L. Shuquan, *Nano Energy*, 2018, **51**, 579–587.
16 L. Zhang, R. Wang, M. Wang, D. Fang and J. Yi, *Chem. Eng. J.*, 2023, **475**, 146127.
17 L. Zhang, D. Fang, F. Wang, J. Yi, M. Wang, T. Hu and Y. Zhao, *Chem. Eng. J.*, 2025, **506**, 159920.
18 X. Wang, A. Naveed, T. Zeng, W. Tao, Z. Hanwei, Z. Yu, D. Aichun, S. Mingru, L. Yunjian and C. Dewei, *Chem. Eng. J.*, 2022, **446**, 137090.
19 Y. Zhao, S. Liang, X. Shi, Y. Yang, Y. Tang, B. Lu and J. Zhou, *Adv. Funct. Mater.*, 2022, **32**, 2203819.
20 Y. Zheng, C. Tian, Y. Wu, L. Li, Y. Tao, L. Liang, G. Yu, J. Sun, S. Wu and F. Wang, *Energy Storage Mater.*, 2022, **52**, 664–674.
21 B. Z. Wu, C. Lu, F. Ye, L. Zhang, L. Jiang, Q. Liu, H. Dong, Z. Sun and L. Hu, *Adv. Funct. Mater.*, 2021, **31**, 2106816.

22 S. Grimme, *J. Comput. Chem.*, 2006, **27**, 1787–1799.
23 M. Bao, Z. Zhang, X. An, J. Liu, J. Feng, B. Xi and S. Xiong, *Nano Res.*, 2023, **16**, 2445–2453.
24 Q. Zong, Q. Wang, C. Liu, D. Tao, J. Wang, J. Zhang, H. Du, J. Chen, Q. Zhang and G. Cao, *ACS Nano*, 2022, **16**, 4588–4598.
25 W. Yang, L. Dong, W. Yang, C. Xu, G. Shao and G. Wang, *Small Methods*, 2020, **4**, 1900670.
26 Q. Zang, X. Cheng, S. Chen, Z. Xiao, K.-P. Wang, L. Zong, Q. Zhang and L. Wang, *Nano Energy*, 2024, **122**, 109301.
27 Q. Li, X. Rui, D. Chen, Y. Feng and S. Huang, *Nano-Micro Lett.*, 2020, **12**, 67.
28 K. S. Maiti, *Chem. Phys.*, 2018, **515**, 509–512.
29 Q. Zong, Q. Q. Wang, C. Liu, D. Tao, J. Wang, J. Zhang, H. Du, J. Chen, Q. Zhang and G. Cao, *ACS Nano*, 2022, **16**, 4588–4598.
30 J. Cuadros, C. I. Sainz-Díaz, R. Ramirez and A. Hernandez-Laguna, *Am. J. Sci.*, 1999, **299**, 289–308.
31 Y. Zhao, S. Liang, X. Shi, Y. Yang, Y. Tang, B. Lu and J. Zhou, *Adv. Funct. Mater.*, 2022, **32**, 2203819.
32 J. Cao, T. Ou, Y. Sun, H. Wu, D. Luo, C. Yang, L. Zhang, D. Zhang, X. Zhang and J. Qin, *J. Colloid Interface Sci.*, 2024, **665**, 32–40.
33 Z. Zhang, B. Xi, X. Wang, X. Ma and S. Xiong, *Adv. Funct. Mater.*, 2021, **31**, 2103070.
34 Z. Cai, H. Wang, T. Wu, H. Ji, Y. Tang, Q. Zhang, Z. Peng and H. Wang, *Mater. Today Energy*, 2024, **43**, 101592.
35 Y. Xiao, J. Ren, M. Li, K. Xiao and Y. Wang, *Chem. Eng. J.*, 2023, **474**, 145801.
36 X. Hu, S. Gao, T. Lin, X. Peng, Y. Huang, Y. Zhang, X. Yang, L. Wang, G. Luo, Z. Wen, B. Johannessen, S. Wang, L. Wang and B. Luo, *Adv. Mater.*, 2025, **37**, 2416714.
37 S. Dolabella, A. Borzì, A. Dommann and A. Neels, *Small Methods*, 2022, **6**, 2100932.
38 M. Hytch, E. Snoeck and R. Kilaas, *Ultramicroscopy*, 1998, **74**, 131–146.
39 D. Zhang, Y. Chen, X. Zheng, P. Liu, L. Miao, Y. Lv, Z. Song, L. Gan and M. Liu, *Angew. Chem., Int. Ed.*, 2025, **64**, e202500380.
40 H. Kato, Y. Kobayashi and H. Miyashiro, *J. Power Sources*, 2018, **398**, 49–54.
41 H. Jiang, Y. Zhang, M. Waqar, J. Yang, Y. Liu, J. Sun, Z. Feng, J. Sun, Z. Pan and C. Meng, *Adv. Funct. Mater.*, 2023, **33**, 2213127.
42 J. Guo, Y. Li, J. Meng, K. Pedersen, L. Gurevich and D. I. Stroe, *J. Energy Chem.*, 2022, **74**, 34–44.
43 Y. Cai, R. Chua, S. Huang, H. Ren and M. Srinivasan, *Chem. Eng. J.*, 2020, **396**, 125221.
44 P. He, G. Zhang, X. Liao, M. Yan and L. Mai, *Adv. Energy Mater.*, 2018, **8**, 1702463.
45 H. Yang, W. Zhou, D. Chen, J. Liu, Z. Yuan, M. Lu, L. Shen, V. Shulga, W. Han and D. Chao, *Energy Environ. Sci.*, 2022, **15**, 1106–1118.
46 Q. Zong, W. Du, C. Liu, H. Yang, Q. Zhang, Z. Zhou, M. Atif, M. Alsalhi and G. Cao, *Nano-Micro Lett.*, 2021, **13**, 116.
47 H. Jiang, Y. Zhang, Z. Pan, L. Xu, J. Zheng, Z. Gao, T. Hu and C. Meng, *Electrochim. Acta*, 2020, **332**, 135506.
48 C. Zhang, Y. Huang, X. Xu, Z. Chen, G. Xiao, Y. Zhong, X. Wang, C. Gu and J. Tu, *Energy Environ. Sci.*, 2024, **17**, 4090–4103.
49 T. Shi, Z. Song, C. Hu, Q. Huang, Y. Lv, L. Miao, L. Gan, D. Zhu and M. Liu, *Angew. Chem., Int. Ed.*, 2025, **64**, e202501278.
50 W. Du, Q. Huang, X. Zheng, Y. Lv, L. Miao, Z. Song, L. Gan and M. Liu, *Energy Environ. Sci.*, 2025, **18**, 6540–6547.
51 N. Liu, X. Wu, L. Fan, S. Gong, Z. Guo, A. Chen, C. Zhao, Y. Mao, N. Zhang and K. Sun, *Adv. Mater.*, 2020, **32**, 1908420.
52 X. Wang, B. Xi, Z. Feng, W. Chen, H. Li, Y. Jia, J. Feng, Y. Qian and S. Xiong, *J. Mater. Chem. A*, 2019, **7**, 19130–19139.
53 X. Liang, L. Yan, W. Li, Y. Bai, C. Zhu, Y. Qiang, B. Xiong, B. Xiang and X. Zou, *Nano Energy*, 2021, **87**, 106164.
54 M. Song, H. Tan, D. Chao and H. J. Fan, *Adv. Funct. Mater.*, 2018, **28**, 1802564.
55 Q. Zhang, S. Ju, S. Zhang, S. Xu and Z. Zhang, *Adv. Energy Mater.*, 2025, **15**, 2404597.